# AUTOMATED IMAGE MOSAICKING

Victor Jung-Der Tsai* and Ying-Ting Huang

## ABSTRACT

This paper developed and implemented automated image mosaicking procedures to produce seamless and smooth mosaics from random sequences of digital aerial images and satellite images. The procedure employs automated algorithms for global image registration, seam line extraction, radiometric adjustment, and composition of overlap images. Results of the experimentation on mosaicking black and white ortho-rectified aerial images and on mosaicking multi-resolution color infrared SPOT-2 and Landsat-5 satellite images show that the implementation of automated conjugate point extraction and image matching algorithms automates the establishment of geometric registration among overlapped images, while the seam line selection and two-step look-up table histogram matching approaches facilitate creating globally smooth and qualitative mosaics. The system developed in this paper makes complex composition of multi-source multi-resolution multi-band images with different geometric and radiometric characteristics an easy and efficient solution for producing reliable mosaic images.

***Key Words:*** image mosaicking, automation, image processing, feature extraction.

## I. INTRODUCTION

Image mosaicking consists of compositing a collection of images to form one continuous view of a large area so that the seam boundaries among the original images are not seen and the mosaic is radiometrically balanced. In general, digital approaches in image mosaicking involve four major tasks: (1) global image registration, (2) seam line extraction, (3) radiometric adjustment, and (4) compositing of adjacent images. Many researchers have published various techniques in each individual step for mosaicking geo-referenced images with overlapping regions. For instance, Fonseca and Manjunath (1996) presented a comprehensive study on the geometric registration techniques for multisensor remotely sensed images. Zobrist *et al.* (1983) proposed techniques for geometric and radiometric corrections along manually selected seam lines for creating large mosaics of Landsat satellite images. Shiren *et al.* (1989) further developed a two-dimensional seam-point search algorithm which takes into account vertical and horizontal edges for reducing artificial discontinuity in the mosaics. Recently, Afek and Brand (1998) integrated global feature-matching algorithms into the process of automatic seam-line selection, margin zone triangulation, and radiometric correction for creating mosaics of ortho-rectified aerial images. Du *et al.* (2001) developed an objective radiometric normalization procedure to create radiometrically normalized image mosaics over a large area using six geo-rectified Landsat Thematic Mapper (TM) images. However, these individual procedures are not fully automated in most commercial software, which usually requires tedious manual intervention at each step. For example, the determination of a pair of images containing overlapped coverage is usually done by manual layout of the images, so is the selection of control image points for establishing the transformation functions of geometric registration and radiometric adjustments.

This paper presents a robust approach to automatic image mosaicking in order to reduce manual intervention in mosaicking sequences of overlapping images. Fig. 1 shows the flow chart of the automatic

*Corresponding author. (Tel: 886-4-22872221 ext. 213; Fax: 886-4-22862857, Email: jdtsai@nchu.edu.tw)

V. J. D. Tsai is with the Department of Civil Engineering, National Chung Hsing University, Taichung, Taiwan 402, R.O.C.

Y. T. Huang is with the Land Survey Bureau, Ministry of the Interior, R.O.C. Taichung, Taiwan 408, R.O.C.

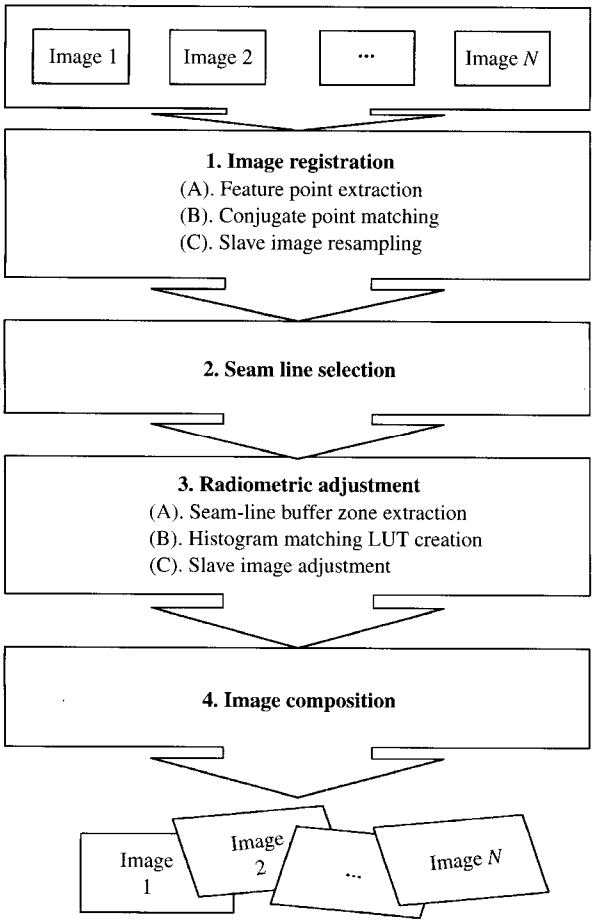


Fig. 1 Operations of the automated image mosaicking system

approach which includes four major steps: (1) image registration, (2) seam line selection, (3) radiometric adjustment, and (4) image composition. In the image registration operation, feature points on each image were extracted by applying interest operators. A sufficient number of pairs of conjugate feature points were then chosen automatically by applying area-based image matching techniques to establish corresponding geometric transformation functions between a pair of overlapping images, followed by resampling the slave image in the pair using bilinear interpolation. In the seam line selection operation, the condition of finding the minimum sum of absolute differences of gray values is used in determining the seam line for merging both images together. In the radiometric adjustment operation, a gray value look-up table of the buffer zones along the selected seam line of both images was then established using histogram matching for adjusting gray values of pixels in the slave image to get close to those of the master image. Finally, in the image composition operation, the master image and the adjusted slave image are tailored together along the seam line to create a seamless and patch-free mosaic with globally smooth appearance. Details and schemes of the proposed automatic approach and experimentation are described in the following sections.

## II. AUTOMATIC IMAGE REGISTRATION

The purpose of image registration is to orientate two or more images with overlapped ground coverage toward the same orientation and pixel sapcing so that they can be combined together. It usually involves three key steps in registering two images, named master and slave images in this paper: (A) extracting feature points in the images, (B) establishing functions of geometric transformation between two images by finding common conjugate feature points in an overlapping region, and (C) resampling the slave image to match the orientation and pixel spacing of the master image. This paper focuses on developing an automatic process for registering blocks of overlapping images, in random sequence, without georeference information. The key task is to determine which two of the images overlap each other by feature extraction and image correlation for conjugate pairs of interest points on adjacent images. Meanwhile, should the images be 3-band color composites, the intensity components of all images are used in steps (A) and (B) for extracting and finding conjugate feature points to establish the geometric transformation functions among overlapped images.

### (A). Feature Point Extraction

The purpose of feature extraction is to extract appropriate features in both master and slave images for finding common points in both images from which corresponding geometric transformation functions can be established. This paper implements automatic extraction of point features in digital images for use as controls in the geometric transformation by adopting the Lue interest operator (Lue, 1988), which is modified from the Förstner operator (Förstner, 1984) and the Moravec interest operator (Moravec, 1975) to reduce its sensitivity to noise. Application of the Lue interest operator includes (a) computing the 4-neighbor gradients of each pixel using a 3 by 3 window, and labeling the pixel as candidate if at least two of the gradients are larger than a user-given threshold; (b) computing the interest value of the candidate pixels as the sum of the absolute value of the 8-neighbor gradients; (c) finalizing the interest points with local maximum interest value by applying the suppression of local non-maximum method (Moravec, 1975) over a user-defined window around each candidate pixel. Though depending on the source images, default threshold of the gradient in step (a) is set as the standard deviation of the input

image and the size of the suppression window in step (c) is set as 40 by 40 in the implementation.

### (B). Conjugate Point Matching

The interest points in each pair of images are exhaustively assessed to find conjugate points with great similarity by applying one of the two area-based image matching techniques at the user's choice: the normalized cross-correlation (NCC) matching technique and the least squares matching (LSM) technique (Wolf & Dewitt, 2000). The NCC method is used for images with similar geometric orientation and pixel spacing due to its limitation in responding appropriately to a number of geometrical and radiometric distortions in image acquisition. On the other hand, the LSM method dominates significantly in matching images with different properties in pixel resolution, frame orientation, projection, and radiometric conditions due to its flexibility and accuracy based on a statistical estimation model. However, the NCC technique is much easier than the LSM technique in computational complexity. Basic concepts of these two matching techniques follow.

*(i) NCC Technique*

Detecting spectral similarity among pairs of images by computing the correlation coefficient in spatial convolution operations of the reference template $f$ in the master image over the search template $g$ in the slave image,

$$r=\frac{\sum_{i=1}^{m}\sum_{j=1}^{n}[(f_{ij}-\overline{f})(g_{ij}-\overline{g})]}{\sqrt{\left[\sum_{i=1}^{m}\sum_{j=1}^{n}(f_{ij}-\overline{f})^2\right]\left[\sum_{i=1}^{m}\sum_{j=1}^{n}(g_{ij}-\overline{g})^2\right]}} \quad (1)$$

in which $f$ is the reference template, with user-defined size, in the master image, $g$ is the search template, with three times the size of $f$, in the slave image, $m$ and $n$ are the size of the reference template, e.g., 11 by 11, $\overline{f}$ and $\overline{g}$ are means of templates $f$ and $g$, respectively, and $r$ is the cross-correlation coefficient as the similarity indicator between the master and the slave image templates.

*(ii) LSM Technique*

Minimizing the square sum of the remaining grey value difference between the two homologous image templates $f$ and g by solving the transformation parameters in Eq. (2), that considers both geometric and radiometric variations between the reference template and the search template, using least squares in an iterative process (Gruen, 1996; Wolf & Dewitt, 2000).

$$f(x_t, y_t)=h_0+h_1 g(a_1+a_2x_t+a_3y_t, b_1+b_2x_t+b_3y_t)$$
$$=f(x, y)+V(x, y) \quad (2)$$

in which $h_0$ and $h_1$ are parameters for radiometric transformation, $a_1$, $a_2$, $a_3$, $b_1$, $b_2$, $b_3$ are parameters for geometric affine transformation, and $V(x, y)$ is the residual or the difference between $f(x_t, y_t)$ and $f(x, y)$.

A threshold of similarity in each matching method was applied for ensuring the determination of appropriate conjugate image points, which are then used to solve for the parameters of the geometric transformation in a least squares solution. Geometric transformation such as conformal, affine, polynomial, perspective projection and local rubber-sheet warping can be applied at the user's choice in considering the imaging geometry of the source images compensating for various geometric distortions. However, the number and distribution of conjugate image points in the overlapping area control the quality of the geometric transformation. Therefore, the root-mean-squared errors (RMSE) of the conjugate points in the forward and backward geometric transformations are further used as indicators for iteratively screening out inaccurate false-matched points with large discrepancies in coordinates in the recursive solution of the transformation parameters in both directions. Thus, a reliable registration of the slave image to the master image is assured.

### (C). Slave Image Resampling

To register two images together not only requires establishing the geometric transformation functions of a slave image to a master image, but also demands radiometric interpolation of the transformed slave image. The latter is done in this paper by resampling the pixel values in each band using bilinear interpolation for a smooth appearance of the resampled slave image, which should have the same orientation and pixel spacing as the master image.

## III. AUTOMATIC SEAM LINE SELECTION

Seam line selection is the process of searching seam points in each row in the overlapping region to produce the least amount of artificial edges (Shiren *et al.*, 1989). The artificial edge in image mosaics corresponds to grey value differences between the two overlap source images caused by different radiometric conditions during image acquisition. In this case, the seam points in each row of the overlapping region in both master and slave images were chosen by applying the minimum absolute grey difference sum approach (Shiren *et al.*, 1989).

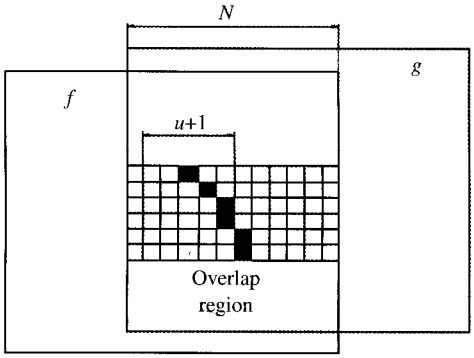


Fig. 2 Seam line selection (*f*: master image, *g*: slave image)

Assume that the pixel grey values of the master image and the resampled slave image are represented by $f$ and $g$, respectively, and the overlap region is $N$ pixels wide specified by the user. As shown in Fig. 2, the sums of the pixels absolute-grey-difference in the $j$-th row over a $u$+1 pixels wide search area within the overlap regions are computed using Eq. (3),

$$v_{j,k} = \sum_{i=-u/2}^{u/2} \left| f_{j,k+i} - g_{j,k+i} \right| \tag{3}$$

for $k$=1, 2, ···, $N$. The seam point position, i.e., $k^*$, is determined for the $j$-th row by finding the minimum value of $v_{j,k}$. However, the search of seam points in this way is one-dimensional (1-D) and may find a succession of random points, with unrelated pixel positions, which will introduce discontinuity between adjacent rows. If the horizontal shift of seam points in successive rows is significant, a horizontal artificial edge is eventually introduced into the mosaics. In order to eliminate the horizontal edges, the range for the candidate seam point in the ($j$+1)-th row is limited in [$k^*$-$s$, $k^*$+$s$] where $s$ is a function of $v_{j,k}$ (Milgram, 1975). Usually, default values of 20 and 30 for $u$ and $s$ of the seam point search area parameters would find the seam line without abrupt artificial edges. As with the image registration steps (A) and (B), the intensity components are used to find the seam line between the overlapped 3-band color composite images.

## IV. AUTOMATIC RADIOMETRIC ADJUSTMENT

The purpose of radiometric adjustment is to diminish the discontinuities along the seam line and the radiometric difference between the two images for creating a smooth and seamless mosaic. The difference in contrast of images caused by various solar conditions during image acquisition may lead to patched mosaics with apparent seam lines between two patches of image with different contrasts. In order to reduce the radiometric difference between the master and slave images, a linear stretch approach is usually applied prior to the image registration to match the average grey-levels of both images (Hord, 1982; Huang, 1992). On the other hand, a linear grey-level interpolation approach has been widely used over the buffer zones along the seam line to eliminate vertical discontinuities (Murai *et al.*, 1980; Shiren *et al.*, 1989; Afek and Brand, 1998). This method can adjust the pixel intensities of the buffer zones along the seam line for a continuous transition from the left image to the right image. However, it will further introduce two new vertical edges, i.e., boundaries of the buffer zones, to the mosaics even if global image enhancement was used prior to the mosaicking.

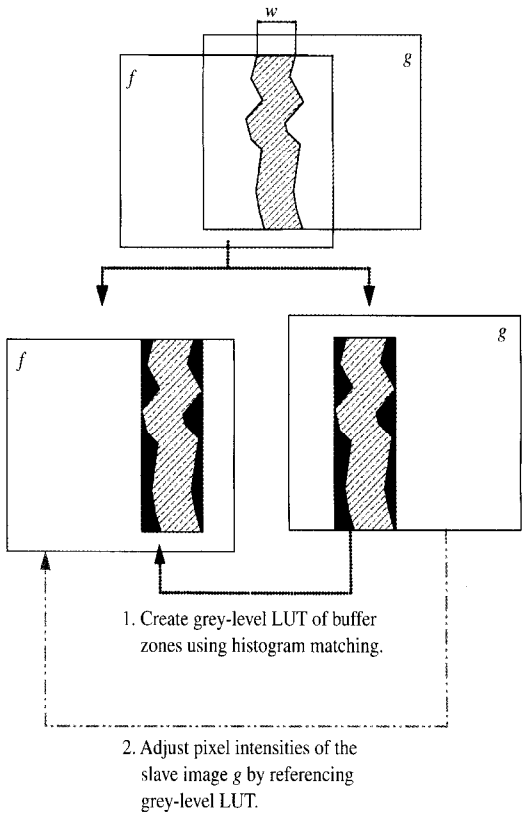


Fig. 3 Two-step radiometric adjustment by histogram matching

This paper implements two-step histogram matching for creating a seamless mosaic with global balance in radiometric intensities. As shown in Fig. 3, the histogram matching method in Richard and Jia (1999) was applied to create a grey-value look up table (LUT) of the buffer zones of $w$ pixels wide along the seam line in both images, band by band from the resampled slave image $g$ to the master image $f$. The width of the buffer zone, i.e., $w$, can be set as the width of the seam line search area, i.e., $u$+1, in the

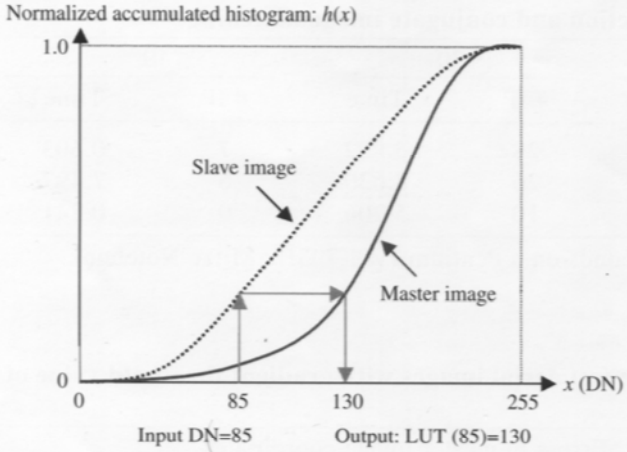


Fig. 4 Grey-level LUT generation using normalized accumulated histograms

seam line selection step described above. Should the overlap area be wide enough, a large value of $w$, e.g., 200, should be chosen to accomplish the best global radiometric balance. Fig. 4 shows the schematic process of generating the grey-value LUT in which the normalized accumulated histograms of the buffer zones of the master and slave images are used in the interpolation of output grey values. The grey-value LUT was then used to globally adjust the pixel intensities of the slave image to match the contrast of the master image.

## V. AUTOMATIC IMAGE COMPOSITION

Image composition of the master image and the radiometrically adjusted slave image is done in a row-wise operation along the selected seam line. As shown in Fig. 5, pixels from the master image at the left of the seam line and pixels from the adjusted slave image at the right of the seam line in each row are wrapped up together to form the final pixels of the mosaic. Thus, a smooth and seamless mosaic with radiometric integrity is produced.

## VI. IMPLEMENTATION AND EXPERIMENTAL RESULTS

The automatic approaches presented above were implemented in a combined system using MATLAB® programs on personal computers. Fig. 6 shows the versatile patterns of image overlap that can be handled in the computer implementation. The system automatically determines the left image as the master image and the right image as the slave image according to their overlap relationship during the image registration process. To mosaic more than two images, the four steps are repeated for appending the next image found overlapping with the currently

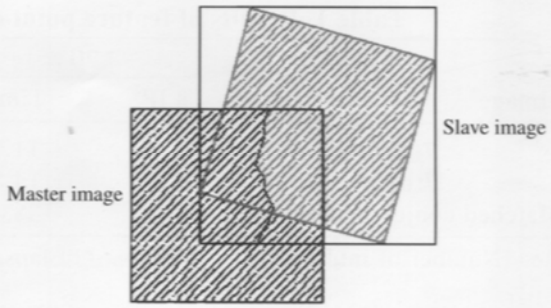


Fig. 5 Image composition along the seam line

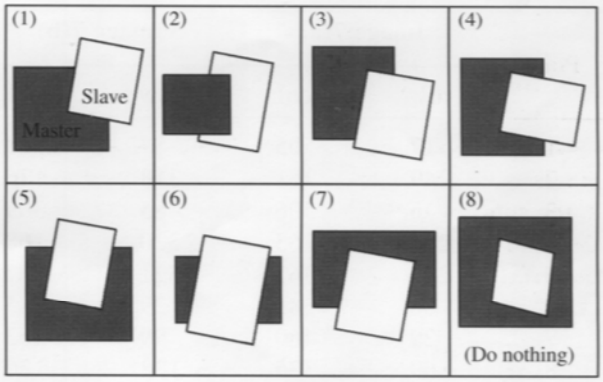


Fig. 6 Cases of image overlap handled in computer implementation

mosaicked image, which is set as the master image hereinafter. However, the user has to specify to the system that the leftmost image is one of the first two images to avoid blank image patches where pixels of the resampled slave image are outside the slave image in image registration.

A set of ortho-rectified black and white aerial images as well as a group of geo-referenced SPOT-2 multispectral (XS) and Landsat-5 Thematic Mapper (TM) color infrared satellite images were used to verify the proposed algorithms in mosaicking grey-level images and color images, respectively. Experimental results and performance analysis of the system are illustrated in the following.

### (A). Black and White Aerial Images

Figure 7 shows the test images which are ortho-rectified subsets of a stereo pair of aerial photographs with different orientations and 80% endlap covering an urban area in Taichung city, Taiwan. Table 1 shows the results of the feature point extraction with gradient thresholds respectively set as 20, 30, and 40 for the test aerial images on a Pentium IV-1.7 GHz Mitak Notebook computer. From the results, the greater the gradient threshold was, the smaller the number of interest points extracted and the shorter the time used

**Table 1 Results of feature point extraction and conjugate image matching**

| Image \ Threshold | 20 | | 30 | | 40 | |
|---|---|---|---|---|---|---|
| | # IP* | Time** | # IP | Time | # IP | Time |
| 7(a) | 77 | 11.161 | 28 | 5.882 | 7 | 0.603 |
| 7(b) | 58 | 14.897 | 26 | 8.630 | 6 | 7.497 |
| Matched conjugate points | 15 | 28.468 | 10 | 5.206 | 0 | 0.241 |

Note: *Number of interest feature points. **Elapsed seconds on a Pentium IV-1.7 GHz Mitac Notebook.

**Table 2 NCC-matched conjugate interest points of the test aerial images with gradient threshold value of 30**

| Point | Image 7(a) | | Image 7(b) | | Errors in master image coordinates | | | Correlation coefficient |
|---|---|---|---|---|---|---|---|---|
| | row | col | row | col | $d_{row}$ | $d_{col}$ | $\sqrt{d_{row}^2+d_{col}^2}$ | |
| 1 | 17 | 505 | 87 | 308 | 0.08 | 0.19 | 0.21 | 0.949 |
| 2 | 249 | 371 | 318 | 176 | 0.19 | 0.09 | 0.21 | 0.986 |
| 3 | 15 | 506 | 85 | 309 | 0.07 | 0.21 | 0.22 | 0.947 |
| 4 | 251 | 363 | 320 | 168 | 0.25 | -0.01 | 0.25 | 0.989 |
| 5 | 252 | 362 | 321 | 167 | 0.26 | -0.02 | 0.26 | 0.989 |
| 6 | 60 | 381 | 129 | 185 | 0.01 | -0.34 | 0.34 | 0.981 |
| 7 | 29 | 460 | 99 | 263 | 0.42 | -0.36 | 0.55 | 0.966 |
| 8 | 69 | 375 | 138 | 180 | 0.05 | 0.58 | 0.58 | 0.991 |
| 9 | 21 | 468 | 90 | 271 | -0.65 | -0.24 | 0.69 | 0.965 |
| 10 | 264 | 358 | 332 | 163 | -0.70 | -0.10 | 0.71 | 0.989 |
| | | | | RMSE: | 0.36 | 0.27 | 0.45 | |

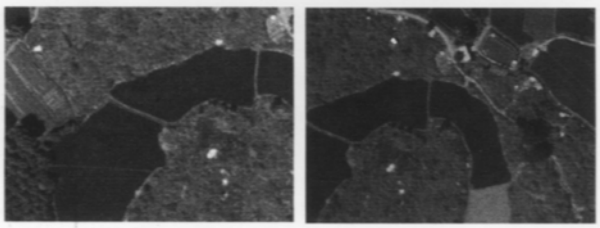

(a) Image A: 374 rows×507 columns (b) Image B: 441 rows×594 columns

Fig. 7 Test ortho-rectified aerial image subsets (displayed at 30% scale)

for each image. There also exists the same trend between the size of the suppression window and the number of interest points found. Considering the number and distribution of feature points in both images, the result from a gradient threshold value of 30 was adopted for finding the conjugate points for registering the slave image to the master image using two-dimensional (2-D) affine transformation and bilinear interpolation. Table 2 shows the result of the ten matched conjugate points between images 7(a) and 7(b) with 11 by 11 reference window, 40 by 40 search window, 0.75 for correlation coefficient using NCC matching, and 0.5 pixels for RMSE in 2-D affine transformation. In seam line selection, the width of the search area within the overlap region was set to 21 pixels ($u$=20), and the range of candidate seam points for the next row was set to 30 pixels ($s$=30). These values are set as defaults for mosaicking black and white images in the system. However, they can be tuned by the user with empirical values for images from different sources.

In radiometric adjustment, buffer zones of 200 pixels ($w$=200) wide to the right along the seam line as shown in Fig. 8 are used to compute the LUT for adjusting grey values of pixels in the resampled image of Fig. 7(b). Fig. 9 illustrates the histograms and statistical characteristics, including means and standard deviations, of the buffer-zone images. The similarity between the histograms and statistics of the master image and the adjusted slave image shows that the histogram matching approach works satisfactorily in adjusting the slave image to composite a smooth and balanced mosaic result as shown in Fig. 10(a). For comparison purposes, Figs. 10(b), 10(c), and 10 (d) respectively represent the mosaics of the test aerial images in handling the overlap region with three other

(a) Buffer zone of Fig. 7(a) (b) Buffer zone of Fig. 7(b) (c) Matched result of (b)

Fig. 8 Buffer-zone images (300 rows × 251 columns) to the right of the seam line of the test aerial image subsets (displayed at 30% scale)

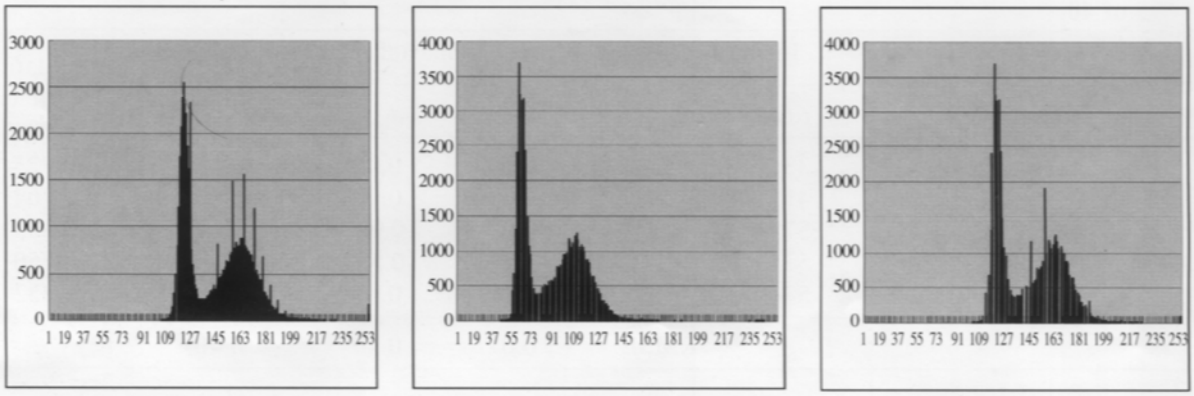


Mean=134.03, Std deviation=26.47 Mean=76.30, Std deviation=26.47 Mean=133.69, Std Deviation=26.80

(a) Master imge (b) Slave image (c) Matchd slave image

Fig. 9 Histograms of buffer zones of the test aerial images

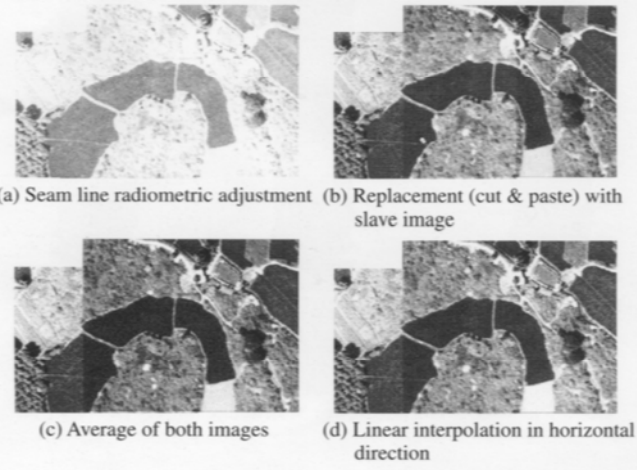

(a) Seam line radiometric adjustment (b) Replacement (cut & paste) with slave image

(c) Average of both images (d) Linear interpolation in horizontal direction

Fig. 10 Mosaics of the test aerial images by various approaches in handling the overlap region (444 rows × 793 columns, displayed at 30% scale)

methods: (1) direct replacement of the master image from the left boundary of the overlay region, (2) average grey value of the pixels within the overlap region, and (3) linear interpolation in the horizontal direction within the overlap region (Murai *et al.*, 1980). Comparing these resulting mosaics, it is shown that no artificial edges can be seen in mosaic 10(a) produced by the proposed approach, nor are patches of different contrasts. However, there are apparent grey-level discontinuities in both vertical and horizontal directions and patches of images in the rest of the mosaics merged by the other methods in handling overlap regions.

### (B). Color Infrared Satellite Images

Figure 11 shows color infrared composites of (a) SPOT-2 XS images and (b) Landsat-5 TM images of bands 2, 3, and 4 in corresponding spectral ranges with respect to the SPOT-2 XS images. The SPOT-2 XS images were collected on October 18, 1996, and the Landsat-5 TM images were collected on October 17, 1996. On level 10 geometric rectifications by the Center for Space and Remote Sensing Research (CSRSR) at the National Central University in Taiwan, both scenes of the SPOT-2 XS and Landsat-5 TM images were resampled so as to have the same orientation but with different pixel spacing of 12.5 and 25.0 meters, respectively.

In the experiments, the SPOT-2 XS image was set as the master while the Landsat-5 TM image was chosen as the slave, respectively. Table 3 shows the results of interest point extraction with gradient thresholds ranging from 30 to 60 and 40×40 suppression

**Table 3 Results of feature point extraction on satellite images with 40×40 suppression window**

| Image \ Threshold | 30 | | 40 | | 50 | | 60 | |
|---|---|---|---|---|---|---|---|---|
| | # IP* | Time** | # IP | Time | # IP | Time | # IP | Time |
| SPOT-2 XS | 243 | 63.391 | 126 | 58.794 | 70 | 47.425 | 28 | 49.247 |
| Landsat-5 TM | 403 | 75.107 | 231 | 46.387 | 89 | 48.423 | 26 | 36.208 |

Note: *Number of interest feature points. **Elapsed seconds on a Pentium IV-1.7 GHz Mitac Notebook.

**Table 4 NCC-matched conjugate interest points of the test satellite images with gradient threshold value of 40**

| Point | Image 11(a) | | Image 11(b) | | Errors in master image coordinates | | | Correlation coefficient |
|---|---|---|---|---|---|---|---|---|
| | row | col | row | col | $d_{row}$ | $d_{col}$ | $\sqrt{d_{row}^2 + d_{col}^2}$ | |
| 1 | 979 | 753 | 334 | 71 | 0.00 | 0.00 | 0.00 | 0.723 |
| 2 | 1156 | 1184 | 415 | 288 | 0.00 | 0.00 | 0.00 | 0.764 |
| 3 | 1478 | 923 | 575 | 138 | 0.01 | -0.09 | 0.09 | 0.835 |
| 4 | 1474 | 927 | 573 | 140 | -0.01 | -0.58 | 0.58 | 0.750 |
| 5 | 1476 | 924 | 574 | 139 | 0.00 | 0.67 | 0.67 | 0.832 |
| | | | | RMSE: | 0.01 | 0.40 | 0.40 | |

(a) SPOT-2 XS image: 1600 rows×1200 columns. (©1996 CNES)

(b) Landsat-5 TM image (bands 2, 3, 4) 1150 rows×1300 columns.

Fig. 11 Test color infrared satellite image subsets (displayed at 15% scale)

Fig. 12 Buffer-zone images (1037 rows × 235 columns) to the right of the seam line of the test color infrared satellite image subsets (displayed at 20% scale) (a) Buffer zone of SPOT-2 XS image; (b) Buffer zone of resampled landsat-5 TM image; (c) Matched result of (b)

window. As with the aerial images, it shows similar trends of relationships between the magnitude of gradient threshold and number of feature points extracted and computational complexity in CPU time. Table 4 shows the matched five conjugate interest points in image registration with threshold for gradient set as 40, 40 by 40 suppression window, 11 by 11 reference window, 40 by 40 search window, 0.70 for correlation coefficient using NCC matching, and 0.5 pixels for RMSE in 2-D affine coordinate transformation. As with the same settings in seam line selection and radiometric adjustment in the aerial images, Fig. 12 shows the buffer-zone images of 200 pixels wide to the right along the selected seam line for computing the LUT to adjust the grey values of pixels in the Landsat-5 TM images. Fig. 13 illustrates the histograms and statistical characteristics of the buffer-zone images of corresponding bands and shows that the histogram matching approach also works very well for multi-band images. Meanwhile, Fig. 14(a) shows the merged mosaic of the SPOT-2 XS image and the Landsat-5 TM image which is seamless and globally smooth in radiometric appearance. It is also shown that no apparent artificial edges or patches are observed in the color infrared multi-source multi-resolution satellite image mosaic produced by the developed system. As with

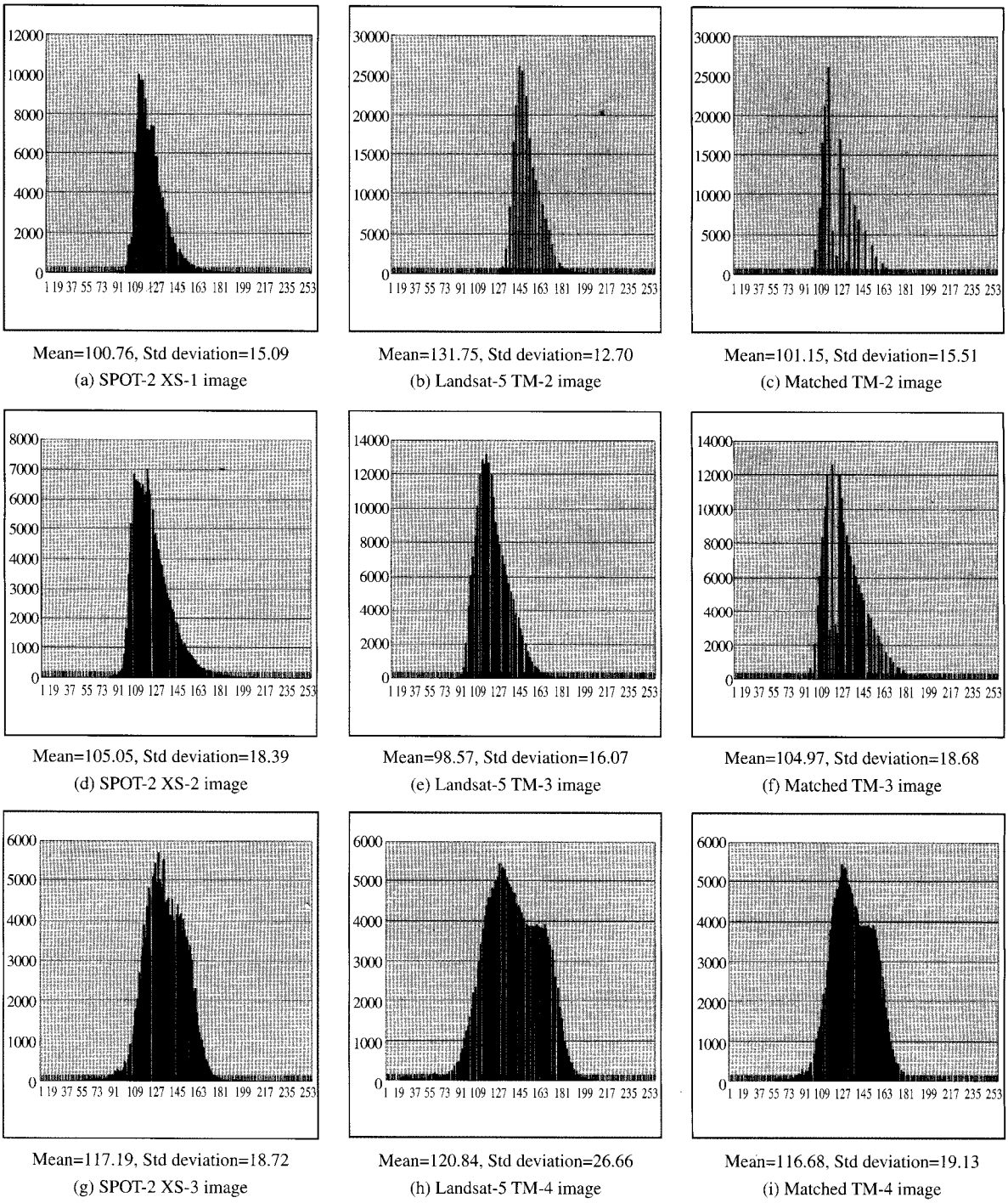


Fig. 13 Histograms of buffer zones of the color-infrared satellite images

the aerial images, there are apparent discontinuities in both vertical and horizontal directions and patches of images in the mosaics merged by the other three methods in handling overlap regions as shown in Figs. 14(b), 14(c), and 14(d), respectively.

From the visual comparison among the resulting mosaics in Figs. 10 and 14, it is shown that the proposed automated system for producing seamless and balanced mosaics is outstanding in eliminating artificial discontinuities, including horizontal, vertical, and seam lines, among images with different radiometric conditions.

### (C). Performance Analysis

The above example images are also used to test

**Table 5 Performance of the automated mosaicking approach in CPU seconds**

| Individual step | Black & white aerial images | | Color infrared satellite images | |
|---|---|---|---|---|
| | CPU seconds | Percentage | CPU seconds | Percentage |
| 1(A). Feature point extraction | 1.141 | 1.80% | 105.180 | 17.50% |
| 1(B). Conjugate point matching | 18.577 | 29.23% | 34.289 | 5.71% |
| 1(C). Slave image resampling | 36.353 | 57.20% | 300.181 | 49.96% |
| 2. Seam line selection | 0.130 | 0.20% | 2.634 | 0.44% |
| 3(A). Buffer-zone extraction | 0.161 | 0.25% | 7.330 | 1.22% |
| 3(B). Histogram LUT creation | 0.060 | 0.09% | 5.379 | 0.90% |
| 3(C). Slave image adjustment | 0.370 | 0.58% | 18.616 | 3.10% |
| 4. Image composition | 6.760 | 10.64% | 127.273 | 21.18% |
| Total | 63.552 | 100.00% | 600.882 | 100.00% |

Note: Based on a Pentium IV-1.7 GHz Mitac Notebook computer running Microsoft© Windows XP®.

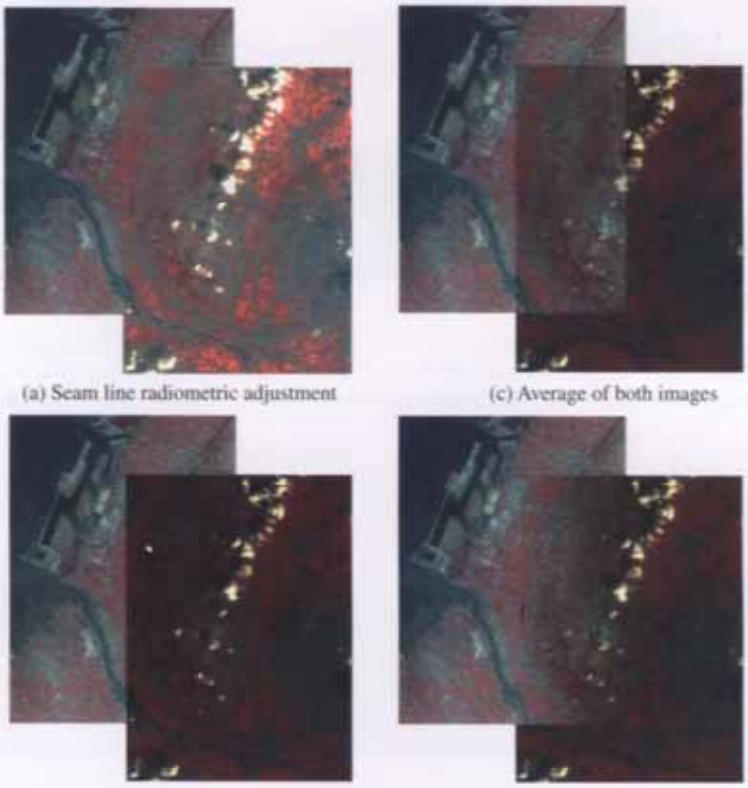

(a) Seam line radiometric adjustment (c) Average of both images

(b) Replacement (cut & paste) with slave image (d) Linear interpolation in horizontal direction

Fig. 14 Mosaics of the test satellite images by various approaches in handling the overlap region (displayed at 15% scale)

the performance of the developed MATLAB® programs running on a Pentium IV-1.7 GHz Mitac Notebook computer. The user is only requested interactively to give the input and output names of the images, parameters such as values of gradient threshold, correlation coefficient threshold, size of master windows in image matching, width of zone for seam line search, and width of buffer zone along the seam line at appropriate stages in operations. Table 5 shows the statistics of CPU time used in each step of the proposed automated system in mosaicking the above-mentioned aerial images and satellite images. For the black and white aerial images, it is shown that 88.2% of the total CPU time of 63.552 seconds was used in image registration, 0.2% in seam line selection, 1.0% in radiometric adjustment, and 10.6% in image composition. For the color infrared satellite images, 73.2% of the total CPU time of 600.882 seconds was used in image registration, 0.4% in seam line selection, 5.2% in radiometric adjustment, and 21.2% in image composition.

Overall, the implementation of automatic conjugate point extraction and image matching algorithms automates and accelerates the establishment of geometric registration among overlapped images, while the implementation of automatic seam line selection and look-up-table histogram matching approaches facilitates producing globally smooth image mosaics. Though the process of exhaustive matching among all interest feature points in large images may be time consuming, an alternative method is to involve some manual interaction to pick up three most distinct corresponding points on both master and slave images for computing preliminary parameters of 2-D affine transformation and let the program do the final tuning with more exact conjugate point pairs by setting a larger search window for image matching.

## VII. CONCLUSIONS

The development in computing technology has led traditional photogrammetric operations towards the digital era, which requires the development of digital image mosaicking approaches, such that the performance and quality of mosaicking is improved. This paper presents automated approaches in image mosaicking processes, including image registration, seam line extraction, radiometric adjustment, and image composition. These procedures were implemented in a combined system in which minimal effort of manual interaction is required for tuning of the parameter settings at appropriate stages in program operations.

Empirical results in compositing black and white aerial images and multi-sensor color infrared satellite images show that the development and implementation of the automated image mosaicking approaches significantly automate and facilitate producing seamless and globally smooth image mosaics for digital image mapping. The system developed in this paper makes complex composition of multi-source multi-resolution multi-band images with different geometric and radiometric characteristics an easy and efficient solution for producing reliable mosaic images.

## ACKNOWLEDGMENTS

The author is gratefully in debt to the anonymous reviewers for their constructive suggestions and comments which make this article and the implemented system for automated image mosaicking more complete than previously.

## NOMENCLATURE

| | |
|---|---|
| $a_i$, $b_i$ | parameters for geometric affine transformation ($i$=1, 2, 3) |
| $f$ | the reference template; the master image |
| $\overline{f}$ | mean of the reference template |
| $g$ | the search template; the slave image |
| $\overline{g}$ | mean of the search template |
| $h_0$, $h_1$ | parameters for radiometric transformation |
| $h(x)$ | normalized accumulated histogram |
| $i$, $j$, $k$ | counting indicators |
| $k^*$ | seam point position in a row of pixels |
| $m$ | number of rows of the reference template |
| $n$ | number of columns of the reference template |
| $N$ | width of overlap region |
| $r$ | correlation coefficient |
| $s$ | number of rows searching downward in seam line selection |
| $u$ | width of search area in a row of pixels in seam line selection |
| $v$ | absolute grey-difference |
| $V(x, y)$ | residual or difference between $f(x_t, y_t)$ and $f(x, y)$ |
| $w$ | width of buffer zone along the seam line |
| $x$ | digital number for image pixel values |
| $(x, y)$ | pixel position in the master image |
| $(x_t, y_t)$ | pixel position in the slave image |

## REFERENCES

Afek, Y., and Brand, A., 1998, "Mosaicking of Orthorectified Aerial Images," *Photogrammetric Engineering and Remote Sensing*, Vol. 64, No. 2, pp. 115-125.

Du, Y., Cihlar, J., Beaubien, J., and Latifovic, R., 2001, "Radiometric Normalization, Compositing, and Quality Control for Satellite High Resolution Image Mosaics over Large Areas," *IEEE Transactions on Geoscience and Remote Sensing*, Vol. 39, No. 3, pp. 623-634.

Fonseca, L. M. G., and Manjunath, B. S., 1996, "Registration Techniques for Multisensor Remotely Sensed Imagery," *Photogrammetric Engineering and Remote Sensing*, Vol. 62, No. 9, pp. 1049-1056.

Förstner, W., 1984, "Quality Assessment of Object Location and Point Transfer Using Digital Image Correlation," *International Archives of Photogrammetry and Remote Sensing*, Vol. 25, Part III, pp. 197-219.

Gruen, A., 1996, "Least Squares Matching: A Fundamental Measurement Algorithm," *Close Range Photogrammetry and Machine Vision*, K. B. Atkinson ed., Whittles Publishing, Scotland, pp. 217-255.

Hord, R. M., 1982, *Digital Image Processing of Remote Sensed Data*, Academic Press, New York, USA, pp. 72-74.

Huang, H. H., 1992, "Seam Smoothing of Digital Color Mosaics," *Archives of the 17th International Society for Photogrammetry and Remote*

*Sensing Congress*, Washington DC, USA, Vol. 29, Part B4, pp. 172-177.

Lue, Y., 1988, "Interest Operator and Fast Implementation," *International Archives of Photogrammetry and Remote Sensing*, Kyoto, Japan, Vol. 27, Part II, pp. 491-500.

Milgram, D. L., 1975, "Computer Methods for Creating Photomosaics," *IEEE Transactions on Computer*, Vol. C-24, pp. 1113-1119.

Moravec, H. P., 1975, "Towards Automatic Visual Obstacle Avoidance," *Proceedings of the International Joint Conference of Artificial Intelligence*, Tokyo, Japan, Vol. 1, p. 584.

Murai, S., Okuda, T., and Akiyama, M., 1980, "Digital Mosaics of Color Aerial Photographs," *Proceedings of the 14th Congress, International Society for Photogrammetry*, Hamberg, Germany, pp. 570-578.

Richards, J. A., and Jia, X., 1999, *Remote Sensing Digital Image Processing*, John Wiley & Sons, New York, USA, pp. 102-106.

Shiren, Y., Li, L., and Peng, G., 1989, "Two-Dimensional Seam-Point Searching in Digital Image Mosaicking," *Photogrammetric Engineering and Remote Sensing*, Vol. 55, No. 1, pp. 49-53.

Wolf, P. R., and Dewitt, B. A., 2000, *Elements of Photogrammetry with Applications in GIS*, 3rd Ed., McGraw-Hill, New York, USA, pp. 334-341.

Zobrist, A. L., Bryant, N. A., and Mcleod, R. G., 1983, "Technology for Large Digital Mosaics of Landsat Data," *Photogrammetric Engineering and Remote Sensing*, Vol. 49, No. 9, pp. 1325-1335.

***Manuscript Received: Aug. 11, 2003***
***Revision Received: Aug. 09, 2004***
***and Accepted: Sep. 14, 2004***